# REPORT DOCUMENTATION PAGE

The public reporting burden for this collection of information is estimated to average 1 hour per response, including the time for reviewing instructions, searching existing data sources, gathering and maintaining the data needed, and completing and reviewing the collection of information. Send comments regarding this burden estimate or any other aspect of this collection of information, including suggestions for reducing the burden, to the Department of Defense, Executive Services and Communications Directorate (0704-0188). Respondents should be aware that notwithstanding any other provision of law, no person shall be subject to any penalty for failing to comply with a collection of information if it does not display a currently valid OMB control number.
**PLEASE DO NOT RETURN YOUR FORM TO THE ABOVE ORGANIZATION.**

| 1. REPORT DATE *(DD-MM-YYYY)* | 2. REPORT TYPE | 3. DATES COVERED *(From - To)* |
|---|---|---|
| 14 July 2008 | Final Performance Report | 14 JUL 2008 - 14 DEC 2011 |

**4. TITLE AND SUBTITLE**

A high-temperature combinatorial technique for the thermal analysis of materials

**5a. CONTRACT NUMBER**

FA9550-08-1-0374

**5b. GRANT NUMBER**

**5c. PROGRAM ELEMENT NUMBER**

**6. AUTHOR(S)**

Prof. Joost J. Vlassak

**5d. PROJECT NUMBER**

**5e. TASK NUMBER**

**5f. WORK UNIT NUMBER**

**7. PERFORMING ORGANIZATION NAME(S) AND ADDRESS(ES)**

School of Engineering and Applied Sciences
Harvard University
Cambridge, MA 02138

**8. PERFORMING ORGANIZATION REPORT NUMBER**

**9. SPONSORING/MONITORING AGENCY NAME(S) AND ADDRESS(ES)**

Air Force Office of Scientific Research
875 North Randolph Street
Arlington, Virginia 22203

**10. SPONSOR/MONITOR'S ACRONYM(S)**

**11. SPONSOR/MONITOR'S REPORT NUMBER(S)**

AFRL-OSR-VA-TR-2012-1078

**12. DISTRIBUTION/AVAILABILITY STATEMENT**

DISTRIBUTION STATEMENT A: Approved for public release.

**13. SUPPLEMENTARY NOTES**

**14. ABSTRACT**

The main objective of the project was to investigate phase transformations in high-temperature shape memory alloys (HTSMA) through use of combinatorial nanocalorimetry. Calorimetry is a powerful characterization tool that is used to study phase transformations and reactions in materials. Nanocalorimetry is a novel variant of this technique in which thin-film and micro-machining technologies are used to fabricate calorimeter sensors that are much more sensitive than traditional calorimeters, that can access a much broader range of heating and cooling rates, and that lend themselves well to combinatorial studies.

**15. SUBJECT TERMS**

| 16. SECURITY CLASSIFICATION OF: | | | 17. LIMITATION OF ABSTRACT | 18. NUMBER OF PAGES | 19a. NAME OF RESPONSIBLE PERSON |
|---|---|---|---|---|---|
| a. REPORT | b. ABSTRACT | c. THIS PAGE | | | |
| U | U | U | U | | 19b. TELEPHONE NUMBER *(Include area code)* |

Reset

**Standard Form 298** (Rev. 8/98)
Prescribed by ANSI Std. Z39.18

# AFOSR Final Performance Report

**Project Title:**  **A high-temperature combinatorial technique for the thermal analysis of materials**

**Award #:**  FA9550-08-1-0374

**Start Date:**  14 July 2008

**Program Manager:**  Dr. Ali Sayir/Dr. Joan Fuller

  Director, High Temperature Aerospace Materials Program

  AFOSR/NA

  801 North Randolph Street, Room 732
  Arlington, VA 22203-1977
  Ali.Sayir@afosr.af.mil
  Joan.Fuller@afosr.af.mil

**Principle Investigator:** Prof. Joost J. Vlassak

  School of Engineering and Applied Sciences
  Harvard University
  Cambridge, MA 02138
  (617) 496-0424
  vlassak@esag.deas.harvard.edu

*Abstract*

This report summarizes the results of the research project performed for the Air Force Office of Scientific Research (AFOSR) under Contract FA9550-08-1-0374, "A high-temperature combinatorial technique for the thermal analysis of materials". The main objective of the project was to investigate phase transformations in high-temperature shape memory alloys (HTSMA) through use of combinatorial nanocalorimetry. Calorimetry is a powerful characterization tool that is used to study phase transformations and reactions in materials. Nanocalorimetry is a novel variant of this technique in which thin-film and micro-machining technologies are used to fabricate calorimeter sensors that are much more sensitive than traditional calorimeters, that can access a much broader range of heating and cooling rates, and that lend themselves well to combinatorial studies.

The first half of the report focuses on the new experimental techniques and capabilities that have been developed as part of this project. A detailed description is provided of the experimental setup that was developed to perform combinatorial measurements. A new ac-scanning calorimetry technique is presented, which is virtually insensitive to heat loss even at elevated temperatures and low scan rates. We also present the first in-situ synchrotron diffraction measurements that can be performed in conjunction with nanocalorimetry for the structural analysis of the samples.

The second half of the report presents experimental results obtained for several materials systems, including the Ni-Ti-Zr and Ni-Ti-Hf high-temperature shape memory alloys and the Au-Si-Cu metallic glass system. Some preliminary results on the formation of $ZrB_2$ coatings through use of reactive multilayers are also presented.

# I. Introduction

This report summarizes the results of the research project performed for the Air Force Office of Scientific Research (AFOSR) under Contract FA9550-08-1-0374, "A high-temperature combinatorial technique for the thermal analysis of materials". The main objective of the project was to investigate phase transformations in high-temperature shape memory alloys (HTSMA) through use of combinatorial nanocalorimetry.

Many titanium-nickel based alloys display shape memory behavior as a result of a thermo-elastic martensitic transformation between a high-temperature cubic phase (austenite) and a low-temperature monoclinic phase (martensite). The shape memory behavior, along with good corrosion resistance, makes these materials suitable for aerospace applications. When fabricated in thin-film form, these alloys can also be used as actuators in micro-electro-mechanical systems (MEMS) [1-6]. TiNi binary thin films are used mainly in low-temperature applications because of their low transformation temperatures (<100°C) [7]. In order to use shape memory-based micro-actuators at elevated temperatures, thin films with higher transformation temperatures need to be developed. Ti-Ni-Hf and Ti-Ni-Zr alloys are promising candidates for this purpose, as they demonstrate both high transformation temperatures (>100°C) and low cost compared to the Ti-Ni-Pd and Ti-Ni-Pt systems [8-11].

Calorimetry is an essential tool in the study of materials that is used to measure transformation temperatures, enthalpies, and heat capacities. It is also used to investigate the kinetics of phase transformations and reactions. Nanocalorimetry makes use of thin-film and micro-machining technologies to significantly reduce the addendum of the calorimeter, enabling ultrasensitive calorimetric measurements [12-15]. It is a proven method for measuring the thermal energies of nanoscale quantities of materials. Nanocalorimetry, in general, possesses characteristics that make it suitable for combinatorial material science: sample fabrication methods are generally compatible with combinatorial sample library fabrication techniques and short measurement times facilitate high-throughput measurements. Thus by combining nanocalorimetry with combinatorial methods, it is possible to efficiently explore phase transformations in complex alloy systems.

The specific research goals of the project include the following: (1) Develop test equipment, sensors, and testing methodology suitable for the calorimetric analysis of high-temperature materials; (2) Prepare combinatorial libraries of thin-film HTSMA alloys using magnetron sputtering; (3) Study the crystallization of and martensitic transformations in combinatorial libraries using combinatorial nanocalorimetry and various structural/phase characterization techniques. The project report is organized as follows: In Section III, we provide a description of the parallel nano scanning calorimeter (PnSC) device that was developed to perform the combinatorial nanocalorimetry measurements and we briefly discuss the underlying theory. In Section IV, we describe in detail the test equipment, sensors, and testing methodologies that were developed as part of this project, greatly expanding the capability of nanocalorimetry. In the Section V, several materials systems including Ti-Ni-Hf, Ti-Ni-Zr, and Au-Si-Cu are analyzed using combinatorial nanocalorimetry and some preliminary work on $ZrB_2$ is discussed. A brief summary is presented in Section VI.

## II. Dissemination of results

The results of this research project have led to 7 publications in archival journals with several more in preparation, to 9 invited or keynote presentations, and several contributed conference presentations. The publications are listed in Section VII.

## III. Parallel nano scanning calorimetry

### A. The PnSC device

The PnSC device consists of a silicon substrate with a number of micromachined nanocalorimeter sensors. The sensors are arranged in a 5 x 5 array to facilitate combinatorial sample preparation (Fig. 1). When a thin-film sample with an in-plane composition gradient is deposited on the substrate, the film is essentially discretized at each sensor, allowing the simultaneous creation of 25 samples with unique composition. The design and operation of the thermal sensors is similar to the nanocalorimeter cells developed by Olson *et al.* [12], with different materials, fabrication method, and geometries. Each nanocalorimeter consists of a thin-film thermistor sandwiched between two electrically insulating silicon nitride layers that form a membrane supported by the substrate [Fig. 2(a)]. The thermistor serves both as a heating element and a thermometer. It is made of tungsten because of its large temperature coefficient of resistance and its small resistivity, both of which are beneficial to measurement sensitivity. The high melting temperature of tungsten also results in excellent thermal stability of the thermistor. The electrical leads and contact pads on the substrate are made of copper to reduce the resistance of the signal lines on the substrate and to facilitate contact to the PnSC device.
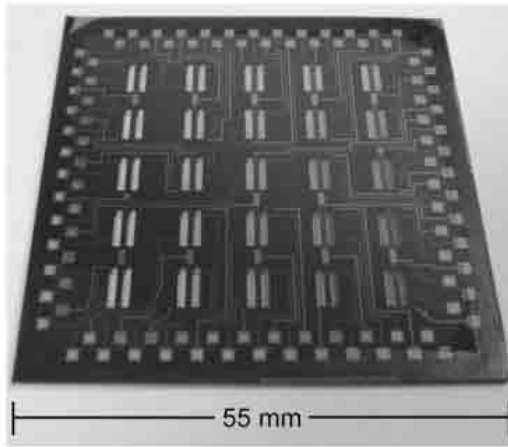


Fig.1 Photograph of the PnSC device

Samples to be measured are limited to the thermistor area of each sensor through use of a shadow mask. The membrane design of the sensor thermally insulates the sample from its surroundings and ensures that the thermal mass of the sensor, i.e., the addendum, is very small. Referring to the schematic in Fig. 2(b), the wide straight line down the center of the membrane is the heating element; the metal lines connected to the heater are the voltage probes, and the portion of the heating element between the voltage probes is the thermistor.

A current passing through the thermistor heats the sample and the calorimetric cell. The power dissipated in the thermistor is determined experimentally from the current supplied to the thermistor and the potential drop between the voltage probes. The local temperature change is determined from a four-point thermistor resistance measurement that has been calibrated to temperature. The calorimetric signal is then calculated from the power dissipated in the thermistor and the heating rate of the sample. Not all power dissipated in the thermistor is used to heat the

3

sample and addendum, however; some of it is lost to the environment. At moderate temperatures, heat transfer from the thermistor to the membrane dominates this heat loss. As the temperature increases, radiation from the thermistor and the membrane becomes important and eventually dominates the heat loss. Measurements are performed in vacuum to eliminate convection losses and to provide a chemically inert testing environment. Conduction and radiation heat losses can be accounted for by modeling or through the use of a reference measurement scheme. In this work, results are generally analyzed using a reference measurement scheme.
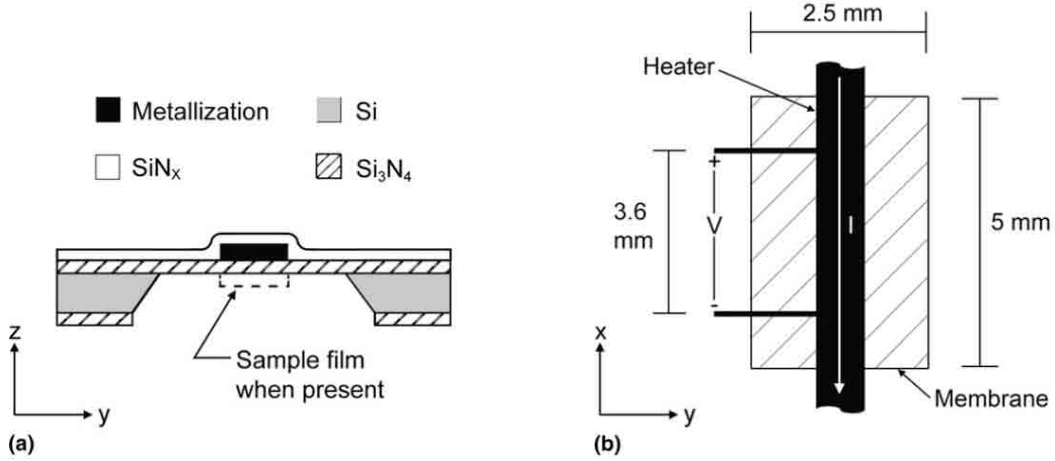


Fig.2    Layout of the nanocalorimeter cell: (a) cross-section schematic, and (b) plan-view schematic. Heater line width is 0.8 mm and voltage probe line width is 0.1 mm.

**B. Operating principle of the PnSC**

The power dissipated in the thermistor can be parsed into power stored in sample and addendum and in power lost to the surroundings. At constant pressure, the stored power results in a change of the enthalpy of the sample and calorimeter addendum. If we define a control volume (CV) that comprises the sample and the calorimeter addendum, then

$$P = H' + Q ,\qquad (1)$$

where $P$ is the total power dissipated in the thermistor, $H'$ is the time rate of change of the enthalpy within the CV, and $Q$ is the heat loss through the boundaries of the CV. The rate of change of the enthalpy can be written as

$$H' = \frac{dH}{dT}\frac{dT}{dt} ,\qquad (2)$$

where $T$ is the temperature of the thermistor. Substituting Eq. (2) into Eq. (1) and rearranging results in

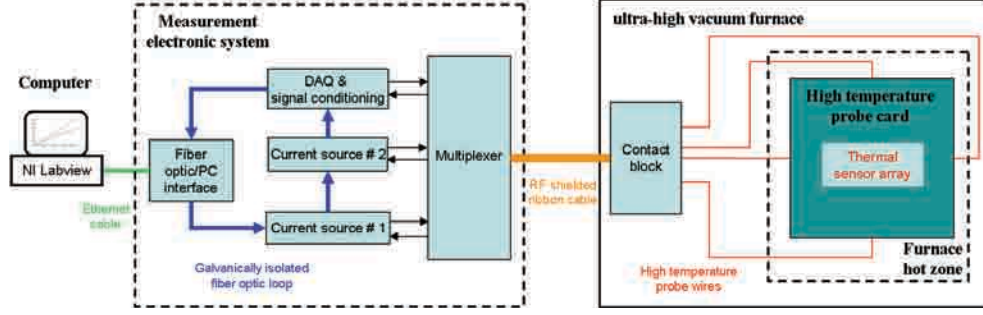$$\frac{P}{T'} = \frac{dH}{dT} + \frac{Q}{T'} ,\qquad (3)$$

4

Fig. 3. Schematic of experimental setup

where $T'$ is the heating rate of the thermistor. The left side of Eq. (3) can be directly calculated from measured quantities and is defined as the calorimetric signal from the sensor. If $Q$ is known or if its contribution to Eq. (3) is negligible (e.g., in the case of large heating rates), the change in enthalpy with temperature, $dH/dT$, can be determined directly from the calorimetric signal. If no phase transformations or reactions take place, $dH/dT$ is equal to the heat capacity $C_P$ of the control volume; during a phase transformation this term also includes the latent heat of transformation $H_L$.

To reduce the effect of the calorimeter addendum and/or heat loss on the measurement, it is convenient to perform a reference measurement. Equation (3) can then be rewritten to define the differential calorimetric signal as

$$\Delta \frac{P}{T'} = \Delta \frac{dH}{dT} + \Delta \frac{Q}{T'} , \tag{4}$$

where $\Delta$ represents the difference between a sensor with a sample and a sensor that is either empty or that contains a reference sample. Comparing measurements in this manner eliminates the contribution of the addendum and reduces heat loss contributions to the signal. If the heating rate of both sensors is identical, then the heat conducted into the membrane is the same for both sensors and the heat loss term in Eq. (4) vanishes. The differential calorimetric signal is the quantity that is analyzed to determine transformation temperatures and latent heats throughout this report. In addition to performing differential measurements, the effect of heat losses can also be reduced by increasing the heating rate of the calorimeter.

## IV. Development of test equipment, sensors, and testing methodologies

As part of this project, special test equipment and hardware were developed to perform combinatorial nanocalorimetry over a broad range of temperatures, from room temperature to approximately 1200°C. A schematic of the equipment setup is shown in Fig. 3. The PnSC device is tested in a high-temperature probe card, which is mounted inside an ultra-high vacuum (UHV) furnace. The UHV furnace system provides a high-temperature and chemically inert ambient for the PnSC sensor, and thus reduces the radiation heat loss associated with testing at very high temperatures. A specially designed control electronics system is used to power the PnSC sensors and to acquire the

5

input/output signals from each sensor. The details of each piece of equipment are described below.

## A. Control electronics

The custom-designed control electronics unit operates as a power supply for the PnSC sensors and as a data acquisition (DAQ) system for the input/output signals from each sensor. Both the power supply and DAQ operations are galvanically isolated to ensure a maximum signal to noise ratio for the acquired signals. The control electronics consists of the following sub-systems as illustrated in Fig. 3: (1) Two independent sets of current sources with current source controllers, used for powering the PnSC sensors and for monitoring the current output; (2) a DAQ controller, used for acquiring the voltage output signals from the PnSC sensors; (3) a multiplexer, used for selection of individual sensors for calorimetry measurements; and (4) a host interface, used for executing write/read command from the user computer through an ethernet cable. The host interface communicates to the current source/DAQ controllers through a galvanically isolated fiber optic loop. Voltage-controlled DC power supplies (Agilent E3630A and E3620A) are used to power the sub-systems. A LabView® program installed on a user computer directly controls the current output and data acquisition processes. A picture of the control electronics system is shown in Fig. 4(a).

The current sources are Howland voltage-to-current converters consisting of three high-precision, low noise operational amplifiers (OPA2227, Texas Instruments, Austin, TX) and a high-output current differential driver (AD815, Analog Devices, Norwood, MA). The current sources have adjustable output ranges (25 mA, 50 mA, 125 mA, 250 mA, and 500 mA) and an output compliance of 25 V. Each current source controller contains an ADA board with two 500 kS/sec, 16-bit A/D converters (ADC) and two high-speed 16-bit single-ended D/A converters (HSDAC). The DAQ controller also contains two ADA boards. Data acquisition occurs on eight simultaneous channels at a maximum rate of 300kHz. All D/A and A/D converters in the current source controller and the DAQ controller are calibrated using precision resistors.

During typical operation, the host interface receives from the user computer a pre-defined digital waveform of input current versus time. A control voltage is sent from the current
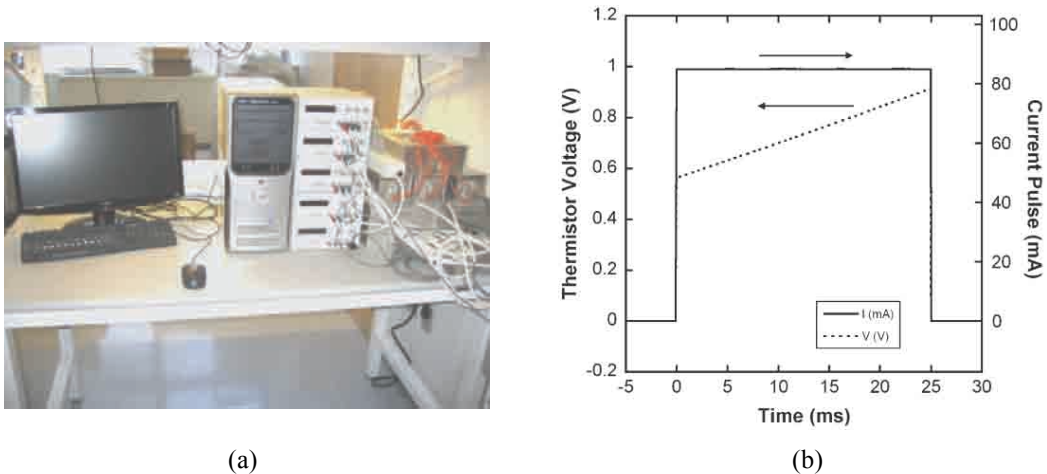


(a)                (b)

Fig. 4. (a) Control electronics system; (b) typical response for a PnSC cell to an 85 mA current pulse.

source controller to the current source. The corresponding current output, after passing through the thermistor on the PnSC sensor, is fed into a precision resistor inside the current source and the voltage drop is measured by the current source controller. The associated voltage output from the PnSC sensor is amplified and digitized by the DAQ controller. Current input and voltage output from the PnSC sensor are dynamically recorded, stored in digital format in a DRAM on the host interface, and eventually transferred to the user computer. A typical current pulse and the corresponded voltage output from a PnSC cell are shown in Fig. 4(b).

## B. Vacuum furnace and high-temperature probe card

Nanocalorimetry measurements are made inside a UHV furnace with an integrated high-temperature probe card. The furnace system is a top loading laboratory furnace (Fig.5) with a nominal base pressure below $10^{-7}$ Torr and an operating temperature ranging from ambient temperature to 1500°C. The hot zone of the furnace consists of a molybdenum mesh heating-element, a molybdenum hearth plate, and multiple layers of molybdenum radiation shields for thermal insulation. The high-temperature probe card is located inside the vacuum furnace hot zone as illustrated in Fig. 6(a). The probe card allows a PnSC substrate to be mounted inside its center cavity so that measurements can be performed at temperature. The probe card is designed to work at temperatures up to 1500°C and has been tested on Si substrates up to 800°C.



Fig. 5. UHV furnace with integrated probe card.

A cross-sectional view of the probe card assembly is shown schematically in Fig. 6(b). The lower and upper plates of the probe card are machined from c-axis single-crystal sapphire. Single-crystal sapphire is used to minimize electrical leakage currents between the probe cards at elevated temperature. High-temperature electrical probes are embedded in the surface grooves on the bottom plate and clamped by the top plate. The probes have
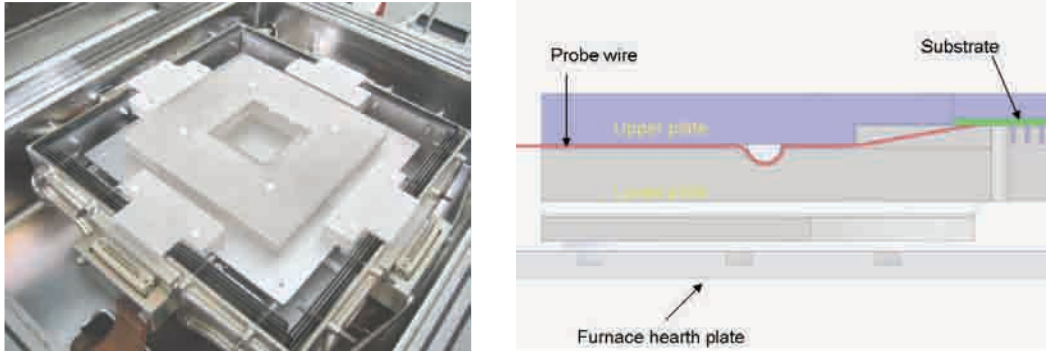


Fig. 6. (a) High-temperature probe card mounted in the hot zone of the UHV furnace; (b) schematic cross-section of the probe card.

a special shape as shown in Fig. 6(b) to ensure good contact with the PnSC pads over the entire temperature range and to avoid buckling of the probes as a result of thermal expansion. The probes are fabricated from a tungsten-25wt.% rhenium alloy to prevent recrystallization and embrittling at elevated temperature. The high rhenium content is also beneficial for the high-temperature tensile strength and creep resistance. Outside the probe card, the high temperature probe wires are connected to contact blocks implemented on the periphery of the hot zone, as shown in Fig. 6(a), which in turn are connected to the control electronics via feedthroughs.

## C. High-temperature PnSC device

The original PnSC device uses a silicon substrate that can withstand background temperatures up to approximately 800°C, with sensor temperatures reaching up to 1200°C. Nanocalorimetry measurements above $1200^\circ$C require a new material set for the PnSC sensor arrays. We have developed a prototype PnSC device that uses a sapphire single-crystal substrate instead of a silicon substrate (Fig. 7) and that can be tested inside the sapphire probe card. Instead of $SiN_x$ membranes with tungsten heating elements, each sensor now consists of a freestanding tungsten filament supported by the sapphire substrate, again arranged in a four-point measurement configuration. The fabrication process starts with a sapphire wafer with an array of pre-machined windows. After the windows in the substrate are filled with a sacrificial resin, the
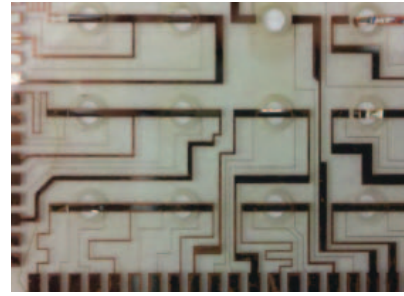
Fig. 7.    Optical image of a sapphire-based PnSC device. The device consists of single-crystal sapphire substrate with pre-drilled cavities and freestanding metal bridges.

metallization is deposited and the substrate is processed using standard photolithography and etch techniques. In a final step, the resin is dissolved in toluene to create freestanding heating elements and the heating elements are coated with a thin layer of $Si_3N_4$ to protect them from oxidation and to electrically insulate them from the samples. After the calorimetry measurements are completed, all coatings can be stripped from the sapphire substrate and the substrate can be reused for future measurements. Figure 7 shows a photograph of the prototype. We anticipate that after further optimization of the device, the maximum measurement temperature for the new sensor array will be around 1700°C. Since the architecture of the new device is very similar to that of the silicon-based device, we expect it to perform similar to the silicon-based device, but at much higher temperatures.

## D. AC nanocalorimetry

One of the drawbacks of scanning calorimetry at very high temperatures or low heating rates is the increased heat loss to the environment, causing the accuracy of the calorimetry measurement to decrease. This problem can be alleviated through use of ac-calorimetry. This technique was first developed by Sullivan and Seidel for bulk materials [15] and consists of supplying an oscillatory heat input to the sample. The resultant sample temperature contains both a dc and an ac component. The amplitude of the

temperature oscillations is inversely proportional to the specific heat of the sample. If the frequency of the heat input is properly selected, the effect of heat loss to the environment can be completely eliminated. We have developed a similar technique for the PnSC device that allows quantitative measurements at much higher temperatures or lower heating rates than scanning calorimetry and that can even be used for isothermal measurements of the heat capacity of a sample.

### *Theory of ac-calorimetry for the PnSC device*

When a harmonic current $I$ is supplied to the heating element in a PnSC sensor,

$$I = I_0 + i\sin\omega t,$$ (5)

the temperature response of the heater can be written as

$$T(t) = T_o(t) + \frac{2iI_0R_0\sin\varphi_1}{\omega C}\cos(\omega t - \varphi_1) + \frac{i^2R_0\sin\varphi_2}{4\omega C}\cos(2\omega t - \varphi_2),$$ (6)

where $T_o(t)$ is a slowly varying function. In this equation, $C$ represents the total heat capacity of the PnSC sensor with sample and $R_0$ is the electrical resistance of the heating element. The phase angles $\varphi_1$ and $\varphi_2$ are given by

$$\tan\varphi_1 = \frac{\omega C}{\alpha - I_0^2 k} \qquad \tan\varphi_2 = \frac{2\omega C}{\alpha - I_0^2 k}.$$ (7)

In these expressions, $\alpha$ is a marginal heat loss coefficient and $k$ is the thermal coefficient of resistance of the heating element. If $\omega$ is chosen sufficiently large, both $\varphi_1$ and $\varphi_2$ approach $\pi/2$ and the amplitudes of the ac-components in Eq. (2) become independent of heat loss. Because of the temperature dependence of the resistance of the heating element, the temperature oscillations of the heater induce $2\omega$ and $3\omega$ signals in the voltage across the heating element given by

$$V_{2\omega} = \frac{5I_0 i^2 R_0 k}{4\omega C}\sin(2\omega t)$$ (8)

and

$$V_{3\omega} = \frac{i^3 R_0 k}{8\omega C}\sin(3\omega t),$$ (9)

for sufficiently large values of $\omega$ and heating rates that are sufficiently small. The amplitudes of these signals are inversely proportional to the total heat capacity of the sensor and sample, and independent of heat loss. Thus a measurement of the amplitudes of the second or third harmonic provides a direct measure for the heat capacity of the sample, independent of any heat loss that may occur.

### *Measurement setup and proof-of-concept measurements*

As illustrated schematically in Fig. 8, the harmonic components of the voltage across the PnSC sensor can be measured using the data acquisition system discussed earlier with the addition of an SRS 650 notch filter. Analysis of the data occurs in the digital domain,

essentially converting the data acquisition system into a digital lock-in amplifier. The system can acquire ac-signals with frequencies as high as 60 kHz.

To develop this measurement technique, mixed ac and dc experiments were performed on a 180 nm Sn coating in the vicinity of the Sn melting temperature. Measurements were performed at a relatively slow heating rate of 500 K/s to aggravate the effect of heat loss. With the data acquisition system functioning as a digital



Fig. 8. Simplified schematic of measurement setup for ac-calorimetry measurements. Signal conditioning and switching electronics not shown.

lock-in amplifier, the dc and $2\omega$ components of the sensor voltage were extracted and used to analyze the calorimetric response. The dc component was analyzed via the traditional scanning calorimetry method in which the enthalpy and heat loss are part of the calorimetric signal. In this experiment, the heat loss of the sensor increased rapidly above 250°C, as evident by the rapidly increasing signal in Fig. 9(a). The dc signal also shows an increasingly worse signal-to-noise ratio in the high-heat loss region. Figure 9(b) shows the calorimetric signal obtained from the $2\omega$ component, which is clearly independent of heat loss. Similar experiments on $ZrB_2$ and Bi coatings over a temperature range from ambient to approximately 800°C confirmed that the calorimetry measurements were not affected by heat loss during the measurement.
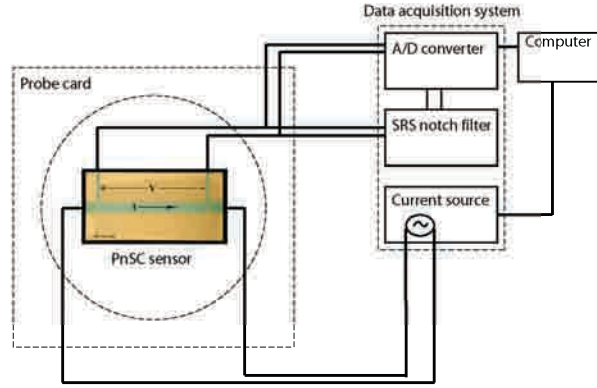


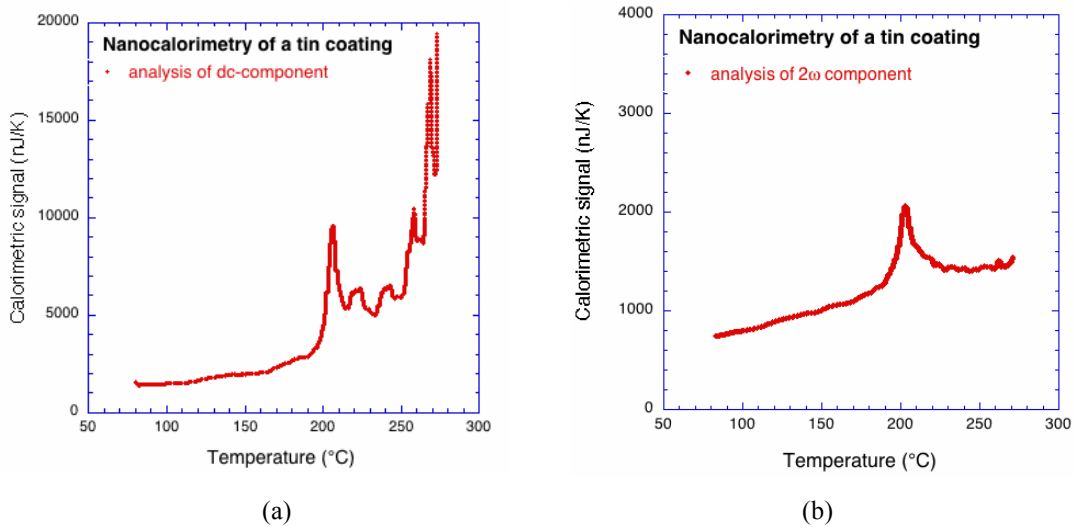(a)                                                              (b)

Fig. 9. Calorimetric analysis of the melting of Sn using a combined dc and ac excitation with (a) the dc and $1\omega$ components and (b) the $2\omega$ components of the sensor response. The calorimetric signal in (a) shows rapidly increasing heat loss at high temperature but the ac-analysis in (b) is independent of heat loss.
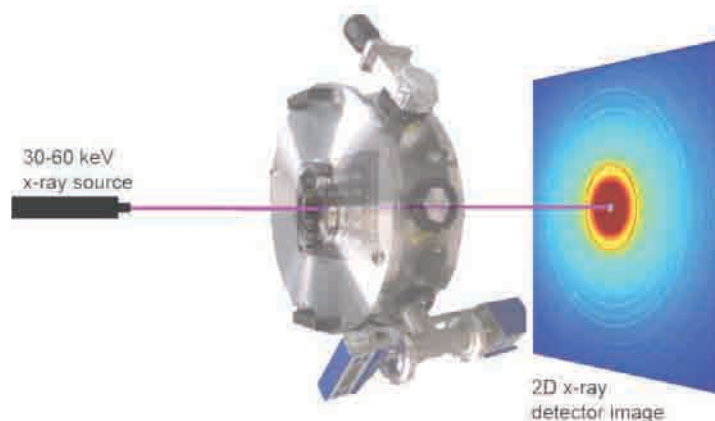
Fig. 10. Schematic of the experimental set-up for in-situ synchrotron diffraction using the PnSC device.

### E. In-situ synchrotron measurements

To complement the calorimetry measurements, we have developed a mobile vacuum chamber that can be used to perform in-situ synchrotron x-ray diffraction during nanocalorimetry measurements. Figure 10 shows a schematic of the experimental setup: it consists of an ultrafast 2D x-ray detector and a small portable vacuum chamber with x-ray transparent windows that houses a probe card for the PnSC device. The chamber is mounted inside the synchrotron hutch such that the x-ray beam shines through a given sample on the PnSC device and the diffracted beams are captured by the detector. The measurement occurs in transmission and produces a diffraction pattern somewhat similar to a typical electron diffraction pattern in a transmission electron microscope. The diffraction data captured in a single exposure is more than that acquired with a several-hours scan on a traditional lab diffractometer.

Our experiments using a flat panel detector (GE 41RT) at the Cornell High Energy Synchrotron Source (CHESS) have shown that up to 10 full diffraction patterns can be acquired per second. This unique capability makes it possible to identify high-temperature phases as they form in the nanocalorimetry sample and to assign calorimetry peaks to specific transformations or reactions. Application of this technique during scanning calorimetry puts an upper bound of approximately 500 K/s on the heating rate. All the diffraction data for the Au-Cu-Si materials system discussed later in this project report were obtained using this experimental setup.

### V. Materials Systems

### A. High-temperature shape memory alloy systems Ni-Ti-Zr and Ni-Ti-Hf

The combinatorial nanocalorimetry technique was used to study crystallization of and martensitic transformations in Ni-Ti-Zr and Ni-Ti-Hf high-temperature shape memory alloy libraries.

*Sample preparation*

Thin-film sample libraries of Ni-Ti-Zr and Ni-Ti-Hf were prepared by DC magnetron sputter deposition in an AJA vacuum chamber with a base pressure in the $10^{-8}$ Torr range. The depositions were performed using three confocal sputter guns with elemental targets, each with a 50.8 mm diameter. The inclination of the individual sputter guns was chosen to create the desired composition gradient across the substrate. The DC power to each gun was determined from an iterative calibration process to obtain the desired composition range. As illustrated in Fig. 11, the samples were deposited through a shadow mask micromachined from a silicon wafer. The shadow mask was formed so that the extrusions in the shadow mask fit into the recesses of the PnSC device and align an opening in the shadow mask with each thermistor on the device. During deposition, the PnSC device and attached shadow mask were held stationary to produce a composition library over the calorimetric cells.
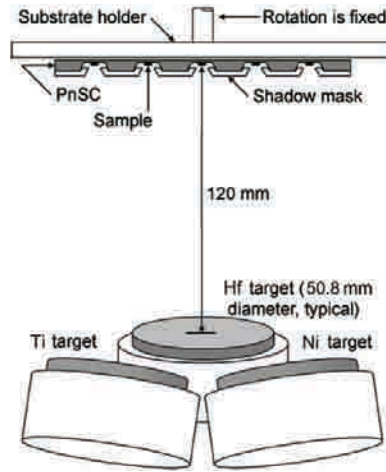


Fig. 11. Schematic of sputter-deposition process

The deposition rate at each sensor location was determined by depositing reference samples on a dummy substrate immediately prior to depositing the calorimetry samples and by measuring the reference sample thickness with a Veeco Detak 6M profilometer. The volume of each sample was calculated from the deposition rate, the area of the shadow mask openings, and the deposition time.

Ni-Ti-Zr samples were sputter deposited to a thickness of 290 nm. The composition of the samples was measured by energy dispersive x-ray spectroscopy (EDS) using an EDAX system installed on a Zeiss Ultra55 field-emission scanning electron microscope. The composition was also measured by wavelength dispersive x-ray spectroscopy (WDS) using a JEOL JXA-8200 Superprobe. Both instruments were calibrated using pure element standards for the Ni–K and Ti–K lines at 15 kV accelerating voltage. For Zr, the L-line was used for EDS and the M-line was used for WDS. Ni-Ti-Zr deposition reference samples were approximately 1 μm thick to ensure accurate composition analysis. Composition measurements were made at the center of each reference sample. Ni–Ti–Hf films were deposited to a thickness of 300 nm. The composition of the Ni-Ti-

Hf samples was determined quantitatively by electron probe micro analyzer (EPMA/JEOL-JXA-8200) using the standard spectra of pure nickel, titanium, and hafnium.

*Crystallization of as-deposited samples of Ni-Ti-Zr*

X-ray diffraction showed that the as-deposited samples of Ni-Ti-Zr (Zr: 15-23 at%, Ti: 28-39 at%) were amorphous. The samples were crystallized by heating the calorimeter sensors to 850°C at a rate of approximately 15 K/ms. Typical calorimetric signals obtained during the crystallization process are shown in Fig. 12(a) for the Ni-Ti-Zr system, along with XRD spectra of the crystallized samples. The crystallization process manifests in various multi-peak calorimetry traces that can be grouped into one of three types as indicated in Fig. 11(a). Figure 12(b) clearly shows each type corresponds to a well-defined range of compositions. Figure 12(b) also shows the temperature of peak crystallization, $T_C$, which occurs between 660 and 735°C, with a minimum around 49% Ni. The lowest temperature recorded for the onset of crystallization (580°C) is well above crystallization temperatures recorded by conventional calorimetry (480°C) because of the fast heating rates in this study. Figure 12(c) shows typical XRD spectra obtained for crystallized Ni-Ti-Zr samples. The crystallization process results in different phase compositions depending on the composition of the samples. The two rows of samples with the lowest Ni content (Group I) contain mainly Ni(Ti,Zr) austenite and martensite. As the Ni content increases, the $Ni_{10}(Zr,Ti)_7$ phase and the intensity of the corresponding peaks increases continuously with increasing Ni content (Group II). While no martensite peaks are detected above 47% Ni, the austenite peaks persists, albeit with reducing intensity as Ni increases. The trends in peak intensity with Ni content hold true in general
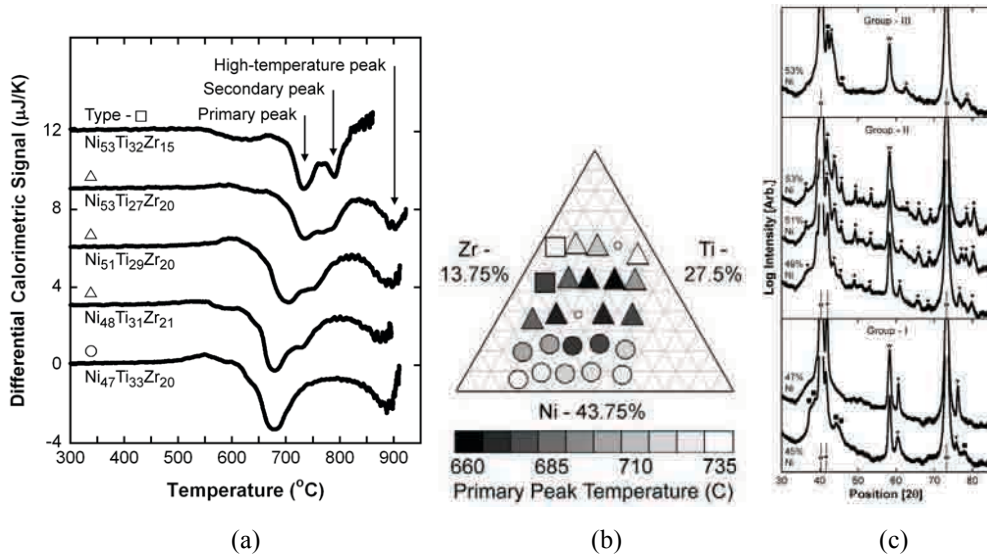


Fig. 12. (a) Examples of crystallization peak shapes in the calorimetric trace of as-deposited samples (offset for clarity). (b) Calorimetry trace type, represented by the ○, △ and □ symbols in (a), and peak crystallization temperature as a function of composition. (c) Examples of XRD spectra. Peaks can be indexed as: tungsten (W) from the calorimeter heating element, Ni(Ti,Zr) austenite (▼), NiTi austenite (▲), Ni(Ti,Zr) martensite (■),(Ti,Zr)$_2$Ni (●), and $Ni_{10}(Zr,Ti)_7$ (◆). Groups correspond to the ○, △ and □ symbols, respectively.

13

except for the two samples with the lowest Zr content: $Ni_{53}Ti_{32}Zr_{15}$ and $Ni_{50}Ti_{34}Zr_{16}$ (Group III). For these samples, the strongest peaks can be indexed as NiTi austenite and $(Ti,Zr)_2Ni$.

### *The martensitic transformation in Ni-Ti-Zr*

A typical calorimetric signal for a crystalline Ni-Ti-Zr sample is shown in Fig. 13(a). The trace shows a strong endothermic peak that corresponds to the transformation of martensite to austenite on heating. The calorimetry traces for the other samples reveal that only samples in the two rows with the lowest Ni content show a martensitic transformation above room temperature. The results are summarized in Fig. 13(b), along with results compiled from Hsieh [16,17]. The transformation temperature varies linearly with Zr content in the range of 16-23%. This result confirms the trend previously reported by Hsieh. The Ni content, by contrast, does not affect the transformation temperature, at least for the samples in which transformations were observed. This behavior is also observed for binary $Ni_xTi_{50-x}$ alloys with $x < 50\%$ [18]. If $x > 50\%$, the transformation temperature decreases by as much as 200°C for a 1% increase in Ni concentration. This behavior, which also occurs in Ni-Ti-Zr [19], may provide an explanation as to why no transformations are observed in the Ni-rich samples – the transformations take place at temperatures well below the measured range.

It is apparent from Fig. 13(b) that the thin-film samples show a marked depression in transformation temperature compared to bulk Ni-Ti-Zr. This depression is caused by the fine microstructure of the samples. SEM observations show that the films in this study have a nanoscale grain structure (10-50 nm diameter) as a result of the fast heating and cooling rates during the crystallization step. A similar depression of the transformation temperature has been demonstrated for NiTi samples with a nanoscale microstructures [20,21] and is attributed to a decrease in the stability of the martensite, related to the



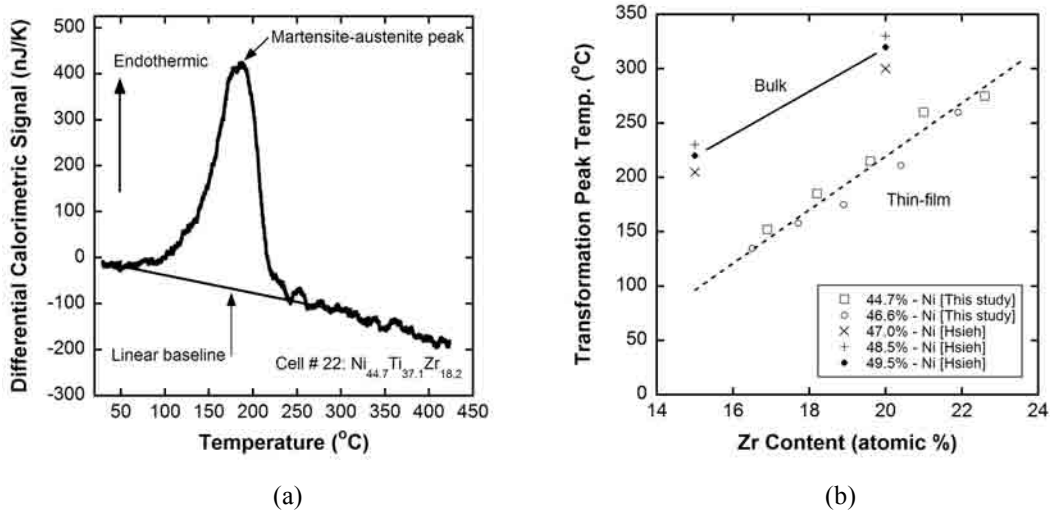(a)                                                    (b)

Fig. 13.    (a) Differential calorimetric signal for the martensite-austenite transformation during heating; (b) Martensite-austenite peak transformation temperatures as a function of Zr content for two the two rows with the lowest Ni content. Results for bulk sample [16, 17] are shown for comparison. Trend lines are drawn as guides to the eye.

energy-cost of forming twin boundaries.

## *Effect of heat treatments on the martensitic transformation in Ni-Ti-Zr*

A typical calorimetric signal of martensitic transformation measured immediately after crystallization can be found in Fig. 13(a). The change of the transformation peak with additional high-temperature heat treatments is depicted in Fig. 14(a). The heat treatments cause a continuous evolution of the peak in the calorimetric signal. The transformation enthalpy – the area under the peak – remains stable for the first few heat treatments and then decreases with additional heat treatments. At the same time, the peak transformation temperature goes through a maximum.

Changes in martensite transformation characteristics have been explained by a precipitation mechanism for bulk Ni-Ti-Zr SMA [17,22] and for films that are several microns thick [23]. Precipitation in Ni-rich NiTi thin films has been shown to follow bulk precipitation for Ni-rich samples, producing metastable and coherent $Ni_4Ti_3$ precipitates with related improvements in shape memory characteristics [24,25]. The growth of these precipitates necessarily changes the composition of the SMA phase, which can result in changes to the martensite transformation characteristics. If the films are Ti-rich, thin films of NiTi can be made to precipitate $Ti_2Ni$ [26]. The shape and orientation of these precipitates depends strongly on composition and the thermal treatment used to create them, with corresponding changes to shape memory characteristics [27].

The trend observed in the M-A transformation results (Fig. 14(a)) with heat treatment can be explained by a similar precipitation mechanism. Initially the precipitates contribute a small volume fraction of the material and their formation causes little change in the composition of the surrounding matrix. The precipitates cause internal stresses that can be relaxed by the self-accommodating twin variants of the martensite phase. The stress relief reduces the overall strain energy and stabilizes the martensite phase over the austenite phase, which increases the transformation temperature during the initial stages



(a)    (b)

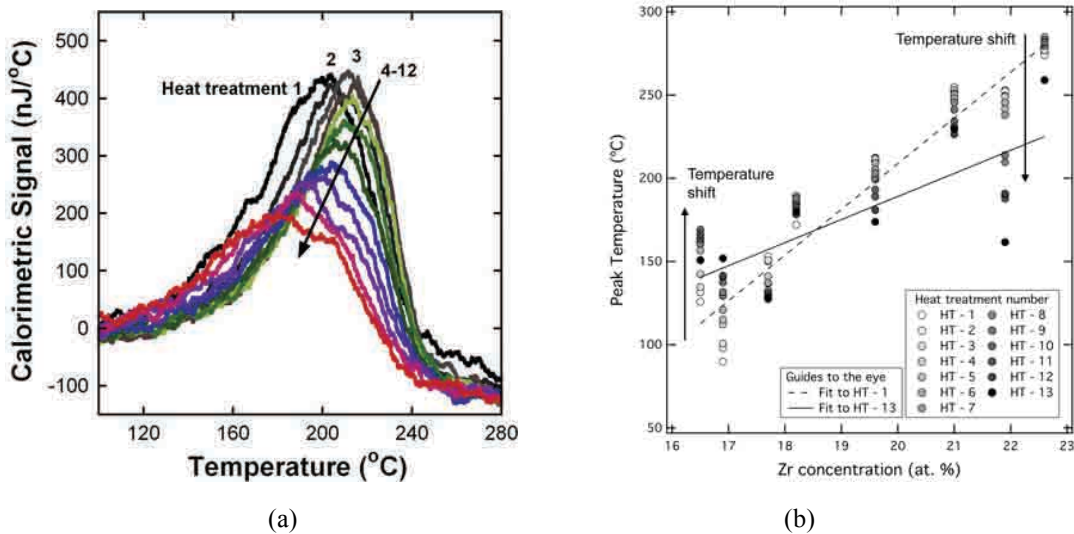Fig. 14:    (a) Evolution of the martensite-austenite transformation peak with high-temperature heat treatments for the $Ni_{44.7}Ti_{35.7}Zr_{19.6}$ sample; (b) Evolution of the martensite-austenite transformation peak-temperature with high-temperature heat treatments as a function of Zr concentration.

15

of evolution. With additional heat treatments, the precipitates continue to nucleate and grow and begin to change the composition of the SMA matrix more significantly. Eventually the effect of the stress becomes less important than the composition shift associated with precipitation. For the sample in Fig. 14(a), this causes the transformation temperature to decrease.
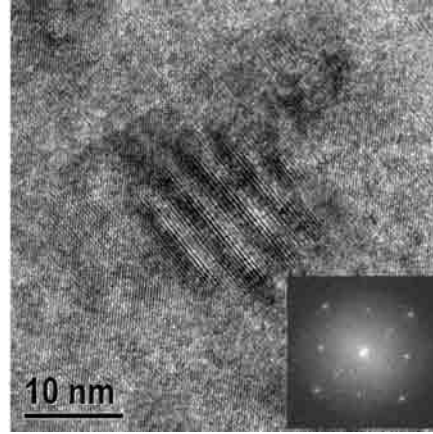


Fig. 15: High-resolution transmission electron micrograph of the NiTiZr sample showing the $Ti_2Ni$ precipitate, determined from the moiré fringes and Fourier transform of the precipitate area (inset) as in [26].

More insight into this mechanism can be gained by considering the effect of HT heat treatments as a function of composition. Figure 14(b) shows the evolution of the transformation temperature with heat treatments as a function of Zr content. At approximately 18.5 at% Zr, there is little change in transformation temperature. Below this composition, the temperature tends to increase, while above this concentration, the temperature decreases. The type of precipitate that forms during the heat treatments depends on the composition of the sample. For samples with a Zr concentration below 18.5 at%, the $Ti_2Ni$ precipitate is expected from the Ni-Ti-Zr ternary equilibrium phase diagram [17]. In fact, the $Ti_2Ni$ base phase was detected in these samples by TEM (Fig. 15) and XRD. For samples with a Zr concentration above 18.5 at%, the equilibrium phase diagram predicts that a Laves phase should precipitate [17]. In these samples, however, formation of the Laves phase was suppressed and $Ni_{10}Zr_7$ formed instead. Since $Ti_2Ni$ is Zr-poor, precipitation of $Ti_2Ni$ causes the Zr content in the SMA phase to increase and therefore increases the transformation temperature. Since $Ni_{10}Zr_7$ is Zr-rich compared to the matrix, precipitation of $Ni_{10}Zr_7$ reduces the Zr content in the SMA phase, thus decreasing the transformation temperature. The trends of the transformation enthalpy with heat treatment are in good agreement with the precipitation explanation.

*Effect of thermal fatigue on the martensitic transformation in Ni-Ti-Zr*

The effect on the martensitic transformation of thermal cycling to 450°C is demonstrated in Fig. 16: The evolution of the transformation peak in the calorimetric signal is shown in Fig. 16(a); the change in transformation temperature is depicted in Fig. 8(b). The transformation temperature decreases with thermal cycling, rapidly at first and then gradually saturating. After heat treatments at 850°C, this thermal fatigue mechanism is reset and the transformation temperature again reduces with thermal cycling.

Thermal fatigue in bulk samples has been attributed to the accumulation of plastic deformation [28,29] during transformation. The strain energy that arises from residual stresses and lattice mismatch stresses at the interfaces of coherent precipitates in austenite is reduced by the formation of self-accommodating martensite. As a result, these stresses
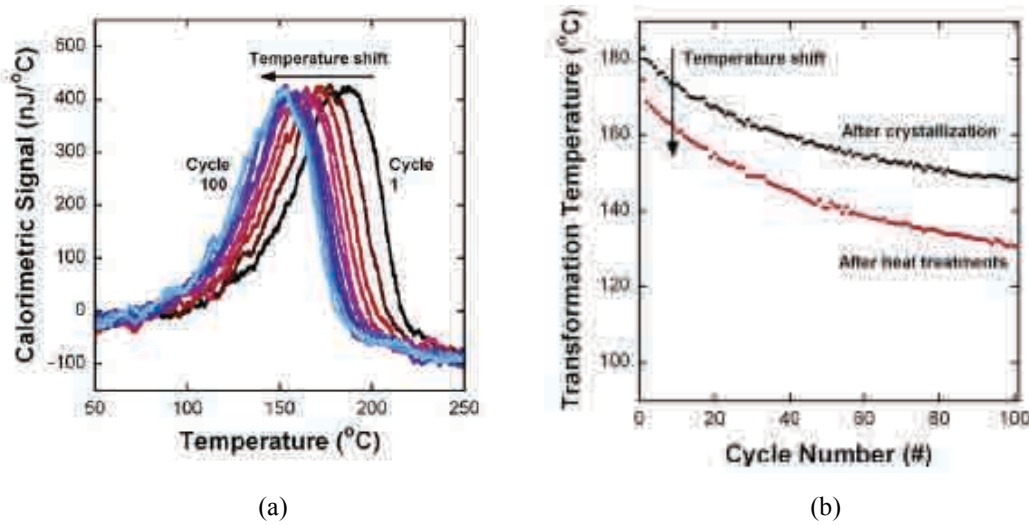
Fig. 16: Thermal fatigue of the martensite-austenite transformation, for the $Ni_{44.7}Ti_{37.1}Zr_{18.2}$ sample, in the calorimetric signal (a), and transformation temperature (b).

tend to stabilize martensite over austenite. During thermal cycling, complex stress fields are developed by the incompatibilities between the martensite, austenite and precipitate phases. These stresses can be large enough to generate dislocations that can relax the internal stresses in the austenite, thus stabilizing the austenite phase and reducing the transformation temperature and enthalpy. The results in Fig. 16 suggest that a similar dislocation-mediated mechanism may be active in the thin-film samples during low-temperature cycling. The figure also demonstrates that the high-temperature heat treatments reactivate the thermal fatigue mechanism, presumably by creating additional stresses due to precipitation or thermal mismatch.

The Ni-Ti-Zr samples in this study are less susceptible to thermal fatigue compared to bulk materials, because the small grain size of the samples makes dislocation formation and activity more difficult than in bulk Ni-Ti-Zr: The volume of material exposed to the large compatibility strains at the martensite-austenite interfaces scales with the martensite twin size. Because of the fine twin structure of the martensite, the volume of material exposed to these large strains is reduced, lowering the likelihood of dislocation nucleation; if dislocations do nucleate, their motion is limited by the small grain size (5-20 nm from TEM). A reduction in dislocation activity due to precipitate pinning was recently shown to increase stress recovery and functional stability in thin films of Ni-Ti-Hf [36]. This result supports the interpretation that additional barriers to dislocation motion, in the present work - grain boundaries, can improve the functional stability of shape memory alloys.

Previous observations of nanocrystalline Ni-Ti have shown that martensite is suppressed in grains smaller than 50 nm in size, even with significant (250°C) undercooling [21,30]. For the Ni-Ti-Zr system, the characteristic martensite twin structure has been observed in the full range of grain sizes, down to the smallest grains (e.g., Fig. 17). These observations suggest that Ni-Ti-Zr is an attractive system for thermal fatigue suppression
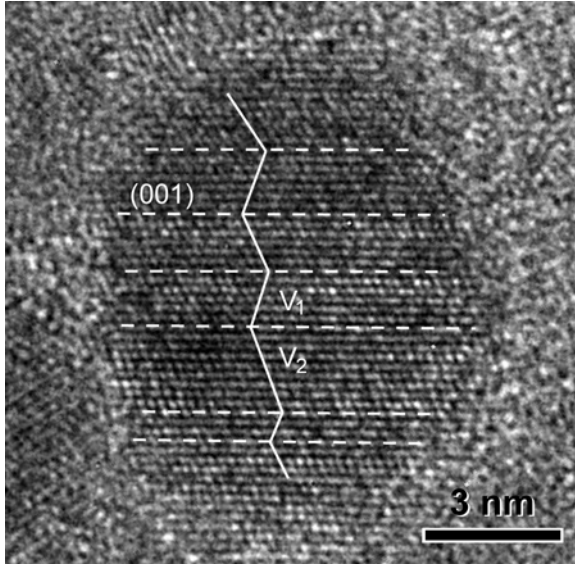
17

Fig. 17: High-resolution transmission electron micrograph of the $Ni_{44.7}Ti_{35.7}Zr_{19.6}$ sample showing (001) compound twins ($V_1$ and $V_2$) in the B19' martensite crystal structure.

by grain refinement because it exhibits B19' martensite at smaller grain sizes than the Ni-Ti system.

When comparing samples across composition, significant differences are observed in fatigue behavior – the $Ni_{44.6}Ti_{32.8}Zr_{22.6}$ sample is particularly stable and appears to be a new level of stability for this materials system. Since the grain size is relatively constant between samples (as determined by TEM and XRD, not shown), grain size effects cannot explain the trends in thermal fatigue with composition or the minimum of thermal fatigue observed in the $Ni_{44.6}Ti_{32.8}Zr_{22.6}$ sample. The trends and minimum of thermal fatigue as a function of composition may be attributed to variations in geometrical compatibility between the austenite and martensite phases. The compatibility between the martensite and austenite phases changes with composition. Previous work has shown that changes in lattice structure caused by variations in alloy composition can be used to tailor interfacial compatibility between the austenite and martensite phases [31]. When the compatibility is maximized, i.e., no distortion at the interface, the stress is minimized. Consequently, the driving force for plastic deformation during the forward and reverse transformations is reduced, as is thermal fatigue. The grain sizes for samples in this study produced broad and overlapping x-ray diffraction peaks, making accurate determination of lattice dimensions difficult. Even so, the $Ni_{44.6}Ti_{32.8}Zr_{22.6}$ composition does provide an intriguing candidate for a lattice compatibility study. Without any additional improvements the $Ni_{44.6}Ti_{32.8}Zr_{22.6}$ material should already be stable enough for some applications, as it shows improved thermal fatigue behavior over reported NiTi binary results [31], a materials system that has seen wide application.

## *Crystallization of as-deposited samples of Ni-Ti-Hf*

Similar to the Ni-Ti-Zr samples, all as-deposited Ti-Ni-Hf (Hf: 13-20 at%, Ti: 31-43 at%) samples were determined to be amorphous by X-ray diffraction. They were crystallized in a 850°C heating cycle. A typical crystallization curve is shown in Fig. 18. The crystallization peak temperature ($658 \pm 2$°C) is significantly higher than previously reported values ($505 \pm 11$°C) for Ti-Ni-Hf films with thicknesses in the micron range [32]. It is also much higher than the crystallization temperature obtained for a freestanding Ti-Ni-Hf film of approximately the same composition using traditional calorimetry ($501 \pm 2$°C). This temperature shift is caused by the kinetics of the crystallization reaction and the very different heating rates used in the measurements

(approximately $1.6 \times 10^4$ K/s for nanocalorimetry versus 10 K/min for traditional DSC). The rise in crystallization temperature can be used in a Kissinger analysis to estimate the activation energy of the crystallization process, leading to a value of approximately 450 kJ/mol, comparable to previous measurements for Ni-Ti-Hf thin films of 487-519 kJ/mol [33].

Figure 19(a) shows a typical TEM micrograph of a sample crystallized using the PnSC. The crystallization process results in a very small ($18 \pm 5$ nm) grain size. The inset



Fig. 18: Calorimetric signal as a function of temperature using the crystallized sample as a reference.

shows the fine twin structure of the martensite that is observed in some of the grains. The grain size in this sample is much smaller than for the freestanding film crystallized using traditional calorimetry ($197 \pm 32$ nm) shown in Fig. 19(b). The small grains formed at grain boundaries of the freestanding film are $(Ti_{1-x},Hf_x)_2Ni$ precipitates.
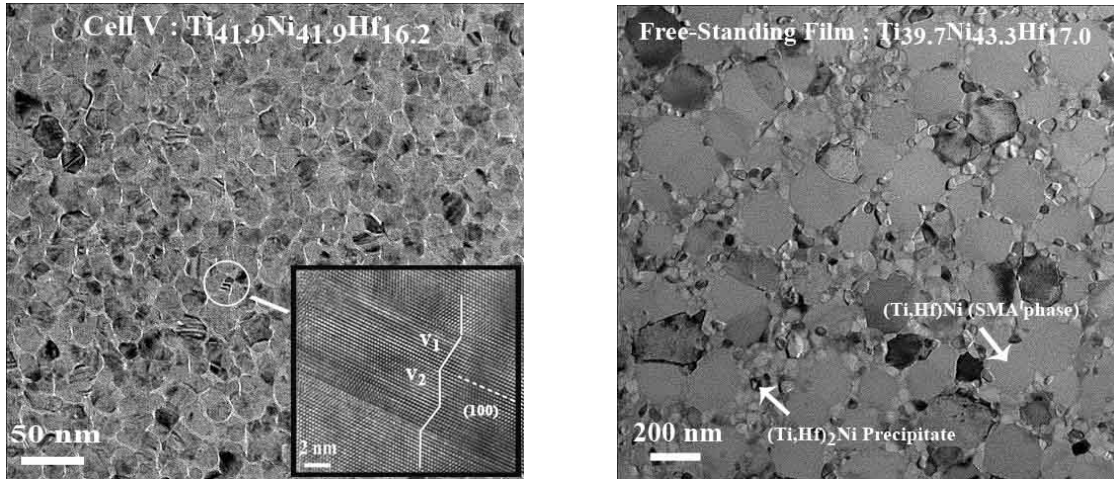


Fig. 19: (a) TEM micrograph of the sample with composition $Ti_{41.9}Ni_{41.9}Hf_{16.2}$ after crystallization using the PnSC; the inset shows a typical high-resolution image of twinned martensite; (b) TEM micrograph of a freestanding film crystallized using traditional DSC.

### The martensitic transformation in Ni-Ti-Hf

The dependence of the martensitic transformation temperature on the Hf and Ni content can be found in Fig. 20. The transformation temperature increases with increasing Hf content, reproducing the trend previously reported for bulk samples by Abujudom and Sanjabi. The Ni content, by contrast, does not affect the transformation temperature significantly as long as the Ni content exceeds 49.3 at%. It is evident from the figure that the transformation temperatures of the 300 nm thin films are lower than for 2 μm films or

19

Fig. 20: Transformation temperature as a function of Hf content. The bulk and thick-film results of Abujudom *et al* and Sanjabi *et al* are also shown for comparison.

bulk samples. Similar to the Ni-Ti-Zr system, this size effect can be attributed to the fine grain structure and even finer twin structure of the samples (Fig. 19(a)).

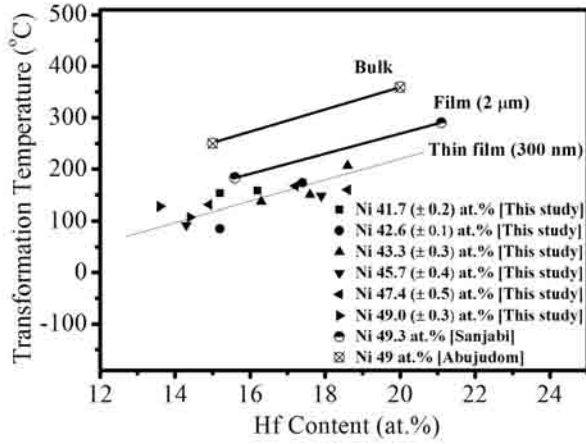Figure 21 compares the transformation curves of samples crystallized by fast scanning on the PnSC device or slow heating in a conventional DSC. The transformation peak is significantly wider for the PnSC measurement. We attribute the broadening of the transformation peak to the small grain size and the heterogeneous microstructure of the PnSC samples. As is evident in Fig. 19, the grain size of the PnSC sample is significantly smaller than for the sample crystallized using traditional means. The relative width of the grain size distributions of PnSC samples is also larger than for traditional samples. When the grain size decreases below 50 nm, the energy barrier to form martensite in TiNi increases significantly due to grain boundary constraints and the twin boundary energy [20,21]. Given that the PnSC samples have a wide distribution of very small grains and that these grains transform at different temperatures, it is not surprising that the transformation peak is much broader than for samples with larger grains.

### Effect of heat treatments on the martensitic transformation in Ni-Ti-Hf

To evaluate the effect of heat treatments on the martensite transformation behavior in the Ni-Ti-Hf system, the PnSC device was used to subject the samples to repeated thermal cycles up to 850°C. A total of twelve thermal cycles were applied to each transforming cell. Depending on the Ni concentration, two distinct trends were observed during cycling:

(a) For Ni ≤ 47 at%, the transformation peak shifts toward higher temperatures with increasing number of cycles. The evolution of the transformation temperature with cycle
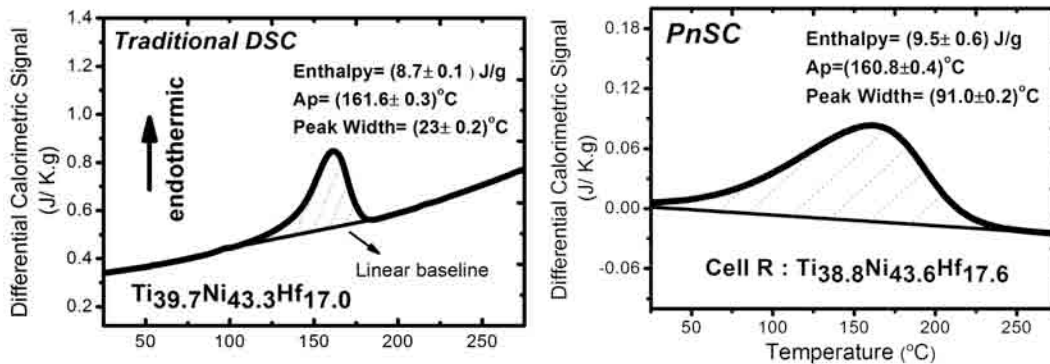


Fig. 21: Comparison of transformation curves for samples crystallized with the PnSC and using traditional DSC.

20

number is illustrated in Fig. 22(a) for all samples demonstrating this behavior. It is evident from the figure that the transformation temperature increases by 30-51°C over twelve cycles. TEM analysis of cell X ($Ti_{38.1}Ni_{43.3}Hf_{18.6}$) shows that the microstructure consists of finely twinned martensite grains and $(Ti_{1-x},Hf_x)_2Ni$ precipitates. Precipitation of the $(Ti_{1-x},Hf_x)_2Ni$ phase increases the Hf content of the matrix and leads to a higher transformation temperature with cycling. A similar mechanism was also observed in the Ni-Ti-Zr films.

(b) For Ni ≥ 47.7 at%, the behavior with thermal cycling is significantly different. Figure 22(b) demonstrates the transformation curve of cell N ($Ti_{35.1}Ni_{47.7}Hf_{17.2}$) as a function of the number of thermal cycles. In this case, the martensite-austenite transformation is gradually suppressed with thermal cycling. Initially a single-stage transformation is observed. As thermal cycling continues, two peaks develop indicative of a two-stage phase transformation. With further cycling, the transformation disappears altogether. Cells O, F and G (Fig. 22(c)) also demonstrate this behavior when subjected to high-temperature cycles. TEM analysis of cell N after the calorimetric measurements shows that this cell consists of austenite (B2), $(Ti_{1-x},Hf_x)_2Ni$ precipitates, and some R-phase. Evidently, precipitation of $(Ti_{1-x},Hf_x)_2Ni$ with cycling enriches the austenite in Ni. Consequently, the sample starts to behave more like the Ni-rich samples of Ti-Ni-Hf library (non-transforming samples). This evolution is indeed observed: the transformation temperature shifts down and the martensitic transformation is suppressed due to the lack of sufficient undercooling.



(a)                                                                 (b)

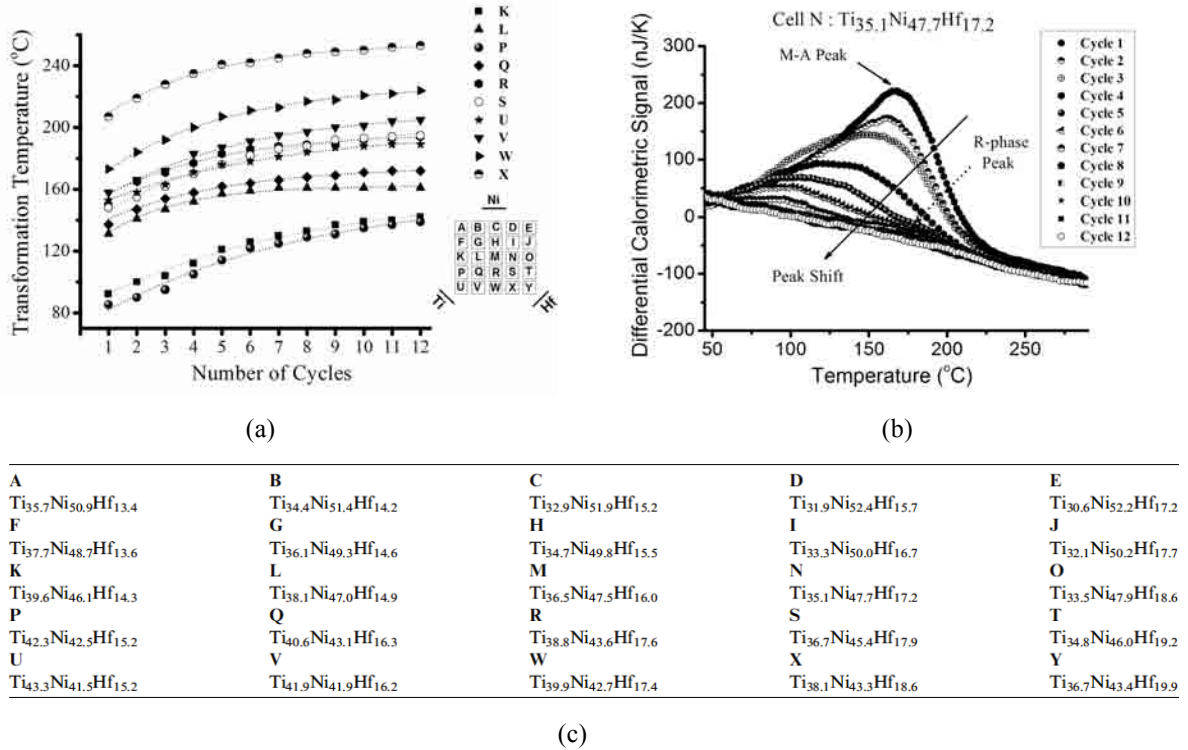| A | B | C | D | E |
|---|---|---|---|---|
| $Ti_{35.7}Ni_{50.9}Hf_{13.4}$ | $Ti_{34.4}Ni_{51.4}Hf_{14.2}$ | $Ti_{32.9}Ni_{51.9}Hf_{15.2}$ | $Ti_{31.9}Ni_{52.4}Hf_{15.7}$ | $Ti_{30.6}Ni_{52.2}Hf_{17.2}$ |
| **F** | **G** | **H** | **I** | **J** |
| $Ti_{37.7}Ni_{48.7}Hf_{13.6}$ | $Ti_{36.1}Ni_{49.3}Hf_{14.6}$ | $Ti_{34.7}Ni_{49.8}Hf_{15.5}$ | $Ti_{33.3}Ni_{50.0}Hf_{16.7}$ | $Ti_{32.1}Ni_{50.2}Hf_{17.7}$ |
| **K** | **L** | **M** | **N** | **O** |
| $Ti_{39.6}Ni_{46.1}Hf_{14.3}$ | $Ti_{38.1}Ni_{47.0}Hf_{14.9}$ | $Ti_{36.5}Ni_{47.5}Hf_{16.0}$ | $Ti_{35.1}Ni_{47.7}Hf_{17.2}$ | $Ti_{33.5}Ni_{47.9}Hf_{18.6}$ |
| **P** | **Q** | **R** | **S** | **T** |
| $Ti_{42.3}Ni_{42.5}Hf_{15.2}$ | $Ti_{40.6}Ni_{43.1}Hf_{16.3}$ | $Ti_{38.8}Ni_{43.6}Hf_{17.6}$ | $Ti_{36.7}Ni_{45.4}Hf_{17.9}$ | $Ti_{34.8}Ni_{46.0}Hf_{19.2}$ |
| **U** | **V** | **W** | **X** | **Y** |
| $Ti_{43.3}Ni_{41.5}Hf_{15.2}$ | $Ti_{41.9}Ni_{41.9}Hf_{16.2}$ | $Ti_{39.9}Ni_{42.7}Hf_{17.4}$ | $Ti_{38.1}Ni_{43.3}Hf_{18.6}$ | $Ti_{36.7}Ni_{43.4}Hf_{19.9}$ |

(c)

Fig. 22:    (a) Variation in martensite transformation temperature as a function of the number of high-temperature cycles; (b) Martensite-austenite transformation peak as a function of the number of thermal cycles for a sample with a Ni content of 47.7 at%; (c) Table with Ni-Ti-Hf sample compositions.

21

## B. Analysis of Au-Cu-Si metallic glass[1]

Metallic glasses (MGs) are under intense investigation due to their desirable mechanical properties including high hardness, yield strength, and low damping coefficient [34-36], and their processibility [37]. While several metallic glass alloys with critical cooling rates below $10^2$ K/s have been developed [35], these systems are typically five component alloys and as such do not lend themselves to easy interpretation of fundamental characteristics of metallic glasses. The majority of ternary glass-forming systems, and in particular ternary Au-based glasses, require higher cooling rates for vitrification, corresponding to time scales that are too fast for traditional calorimetry. However, such time scales are readily accessed by nanocalorimetry, which provides an opportunity to study fundamental properties of metallic glasses. Thus the Au-Cu-Si system was selected as an exemplar to illustrate the unique capabilities of the PnSC device.

### Sample preparation and experiments

An array of 22 devices was simultaneously coated with Au-Si-Cu alloys using co-sputter deposition from elemental targets, producing 175-210 nm thick films with compositions shown in Fig. 23(a). The samples were capped with a 30 nm thick silicon nitride film to protect against sample oxidation in the high-temperature experiments, and during this process, the samples crystallized from their amorphous, as-deposited state. Nanocalorimetry measurements were combined with a combinatorial X-ray diffraction experiment to provide characterization of the crystalline and amorphous components as a function of both quench rate and composition. The XRD measurements were performed at CHESS using the transmission-geometry diffraction experiment (Fig. 23(b)), described earlier. The diffraction patterns were processed to subtract x-ray scattering from sources other than the sample [38], identify Bragg peaks [39], and quantify the diffraction intensity of three identified phases (Fig. 23(c)). In addition to the amorphous phase, which was observed after quenching at rates greater than $10^3$ K/s, an fcc and an intermetallic phase were also observed. The relative concentrations of amorphous and intermetallic phases varied significantly with quenching
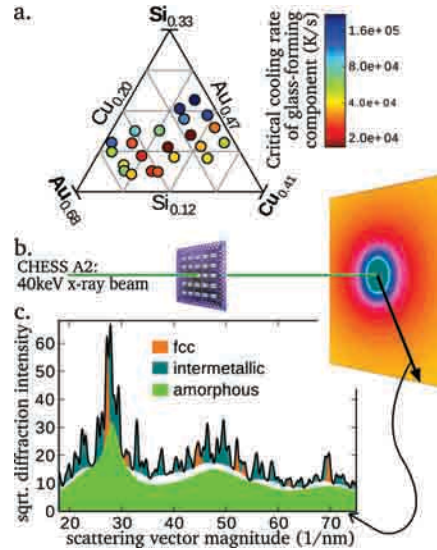


Fig. 23: (a) The 22 sample compositions are shown in a partial Au-Si-Cu composition diagram with the critical cooling rate for complete vitrification of the glass-forming component of the samples. (b) XRD experiment layout is shown with a 40 keV x-ray beam impinging on one of the samples on the PnSC device. (c) XRD diffraction pattern (black line) with colored portions indicating the two crystalline and one amorphous phase.

---

rate, while the fcc phase remained approximately invariant. The crystal structure of the intermetallic phase could not be identified by comparison to diffraction patterns of known phases, and is the subject of continued investigation using bulk samples.

For each calorimetry experiment, a fixed current of 50-100 mA was applied to the device to heat the device and melt the sample. The current was then reduced to 10 mA or lower, allowing the sample to free cool. In the typical vacuum ambient of the PnSC experiment, the cooling rate was approximately $2 \times 10^3$ K/s. To attain increased cooling rates, some measurements were performed in an inert He atmosphere, which increased heat loss and provided free cool quenching rates in excess of $2 \times 10^4$ K/s. Controlled cooling rates of approximately $2 \times 10^2$ K/s were attained by using a larger, but gradually diminishing current during the cooling portion of the experiments.

*Results*

For each quenching experiment, the vitrified fraction of the sample was calculated as the molar fraction of the amorphous phase, normalized by the combined molar fraction of the amorphous and intermetallic phases. Using a total of 65 calorimetry and XRD measurements from different samples and quenching rates, we determined that this vitrified fraction of the glass-forming component increases logarithmically with cooling rate, at approximately 0.4 per decade. Using this trend, the measured vitrified fraction for each sample was extrapolated to unity to attain the critical cooling rate for complete vitrification of the glass-forming component (Fig. 23(a)).

The mapping of critical cooling rate using the PnSC device provides a high-throughput, combinatorial assessment of the glass-forming ability of the intermetallic phase. This ability to directly measure the primary figure of merit for glass forming ability (GFA), the critical cooling rate, will have a significant impact on metallic glass research. The mapping of critical cooling rate over a composition library is useful for establishing composition trends. For instance, Fig. 24(a) shows the Si:Cu ratio of the glass-forming component. Comparison with Fig. 23(a) reveals that the alloys with highest GFA have Si:Cu=0.87. Figure 24(b) shows the variation of the nominal glass transition temperature with composition, revealing a 168-226°C variation among the samples with a strong dependence on Cu concentration. These values are well above the previously measured $T_g$ of 76°C for the similar composition $Au_{55}Cu_{25}Si_{20}$, which is primarily due to the 10,000-fold increase in heating rate [40].
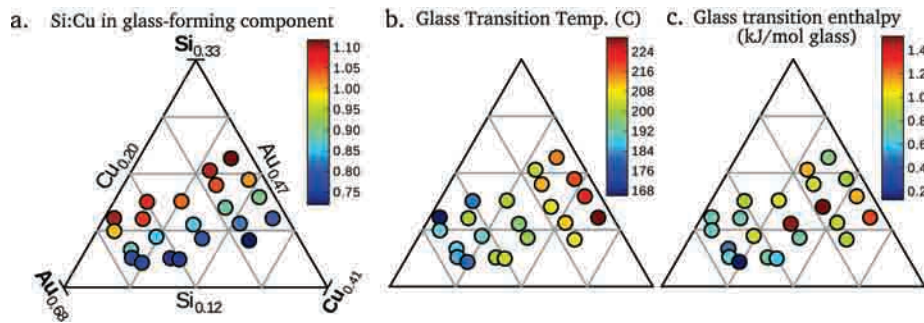


Fig. 24:   Assessed composition trends over the 22-sample library: (a) Si:Cu ratio for the glass-forming component; (b) Glass transition temperature after approximately 2 $10^4$ K/s quench; (c) total enthalpy of the glass transition, normalized by the molar fraction of the amorphous phase.

### Discussion of the glass forming ability

The fast heating and cooling rates offered by nanocalorimetry create unprecedented opportunities for studies of metallic glasses. In traditional metallic glass research, the heating rate of a calorimetry measurement is smaller than the quenching rate, often by several orders of magnitude. In this circumstance, excess free volume in the amorphous metal can be freed in an exothermic relaxation process at temperatures below the glass transition as a result of the appreciable mobility afforded by the low heating rate. After this process, the relaxed glass transforms into a super-cooled liquid structure at $T_g$. In our PnSC experiments, the heating rate exceeds the quenching rate, circumventing structural relaxation of the glass during heating. The ensuing glass transition is fundamentally different from the traditional case as the transition to the super-cooled liquid proceeds directly from the as-quenched isoconfigurational state [41]. This regime of calorimetry experiments offers an opportunity for further investigation into the relationships between free volume and GFA [42-46]. Figure 24(c) shows that the best glass formers in the sample library also exhibit the highest endothermic enthalpy of the glass transition per mole of amorphous material, $\Delta H_g$. This enthalpy is a component of the free energy difference between the glass and super-cooled liquid and scales with the free volume created during the glass transition [47]. A positive correlation of GFA with high density in the amorphous phase has been observed in the Zr-Cu system [42]. A highly dense amorphous structure corresponds to low free volume, which could lead to a relatively large increase in free volume at the glass transition and hence a larger endothermic reaction enthalpy, as observed in our results. While further study is needed to explore the existence and physical basis for this correlation, and in particular how $\Delta H_g$ correlates with free volume in the super-cooled liquid, it is interesting to note the potential to use the $\Delta H_g$ signal as a figure of merit to screen metallic glasses for glass forming ability. This screening method could be employed using traditional calorimetry but it would be particularly effective for combinatorial nanocalorimetry.

## C. Ultra high-temperature ceramics (ZrB$_2$)

As an example of how nanocalorimetry may be used to study ultra-high temperature ceramics, some preliminary work on reactive Zr/B multilayer coatings is presented here.



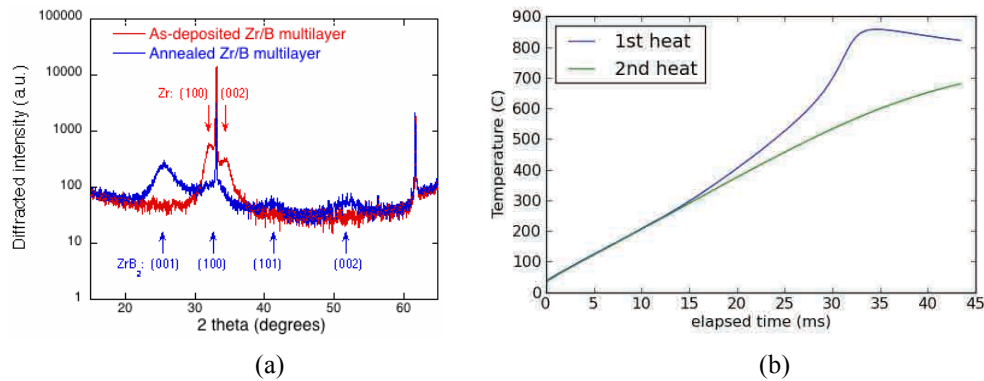(a)                                                                 (b)

Fig. 25:   (a) X-ray diffraction spectra for a 100 nm Zr/B reactive multilayer before and after annealing at 800°C for five minutes. (b) Temperature history for a 130 nm Zr/B multilayer coating (first two thermal cycles). The first cycle shows a distinct exothermic peak, which is absent in subsequent cycles.

Reactive Zr/B multilayer coatings with an average composition $ZrB_2$ were fabricated by sequential deposition of Zr and B layers from elemental deposition sources in a magnetron sputter deposition system. Figure 25(a) shows x-ray diffraction spectra of a multilayer coating before and after annealing at 800°C for five minutes. The spectrum of the as-deposited coating shows the presence of elemental Zr; the absence of distinct B peaks suggests that the sputtered B layers are amorphous. The spectrum of the annealed sample shows diffraction peaks that cor-
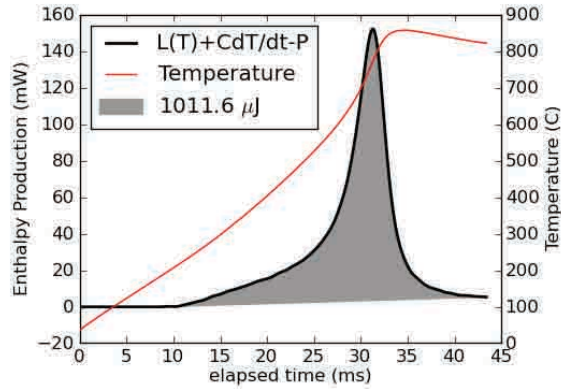


Fig. 26: Enthalpy generated in a reactive Zr/B multilayer as a function of time in the first nanocalorimetry scan, along with the corresponding sample temperature.

respond to the $ZrB_2$ phase, indicating the formation of this phase as a result of the reaction between the Zr and B layers. The temperature history of a 130 nm Zr/B reactive multilayer is plotted in Fig. 25(b) for two thermal cycles performed using a PnSC device. The first scan shows a distinct exothermic peak; subsequent calorimetric scans show no further reactions. Figure 26 depicts the enthalpy generated during the reaction in the first scan, along with the sample temperature. It is evident from the figure that the reaction between B and Zr starts at a surprisingly low temperature of 350°C and peaks around 780°C. This finding should be contrasted with the fabrication of $ZrB_2$ by reactive hot pressing of B and Zr powders, which requires a temperature in the 600°C range [48]. More information on the kinetics of the reaction may be obtained from a detailed analysis of the enthalpy profile and from PnSC scans performed at different heating rates.

## VI. Summary

In this project we have developed the experimental capability of performing high-throughput combinatorial nanocalorimetry measurements over a broad range of temperatures. Structural information on the samples, especially after heat treatments, can be obtained by in-situ synchrotron X-ray diffraction measurements. Measurements at very high temperature are possible through use of ac-calorimetry, which makes the calorimetric measurement virtually immune to heat loss effects, or through use of a sapphire substrate sensor, which allows the background temperature to be raised to minimize radiative heat losses.

The Ni-Ti-Zr and Ni-Ti-Hf shape memory alloys were analyzed as a function of Ni and Zr or Hf content. Transformation temperatures increase with increasing Zr or Hf content and are virtually independent of Ni content as long as the Ni contest does not exceed approximately 50 at%. The transformation temperatures are suppressed compared to those of bulk alloys because of the very fine grain of the samples. The response of these materials systems to high-temperature heat treatments is complex and depends on what phases precipitate out and how they change the Zr or Hf content of the austenitic phase.

The resistance of thin-film samples of these materials systems to thermal fatigue is superior to that of bulk materials.

We have also analyzed the Au-Cu-Si ternary using the PnSC to evaluate its glass forming ability as a function of composition and have identified a range of compositions with a Si-to-Cu ratio of 0.87 that have very good glass forming ability.

## VII. Archival Publications

[1] P.J. McCluskey, J.J. Vlassak, "Nano-thermal transport array: An instrument for combinatorial measurements of heat transfer in nanoscale films", *Thin Solid Films* **518**, 7093-7106 (2010)

[2] P.J. McCluskey, J.J. Vlassak, "Combinatorial nanocalorimetry", *Journal of Materials Research* **25**, 2086-2100 (2010)

[3] P.J. McCluskey, J.J. Vlassak, "Glass transition and crystallization of amorphous Ni-Ti-Zr thin films by combinatorial nanocalorimetry", *Scripta Materialia* **64**, 264-267 (2011)

[4] P. J. McCluskey, C. Zhao, O. Kfir, J. J. Vlassak, "Precipitation and thermal fatigue in Ni-Ti-Zr shape memory alloy thin films by combinatorial nanocalorimetry", *Acta Materialia* **59**, 5116-5124 (2011)

[5] Y. Motemani, P.J. McCluskey, C. Zhao, M.J. Tan, J.J. Vlassak, "Analysis of Ti-Ni-Hf shape memory alloys by combinatorial nanocalorimetry", *Acta Materialia*, in press (2011)

[6] S. Ding, J.M. Gregoire, P.J. McCluskey, J.J. Vlassak, J. Schroers, Solidification of Au-Cu-Si alloys investigated by a combinatorial approach, *Acta Materialia*, submitted (2011)

[7] J.M. Gregoire, P.J. McCluskey, D. Dale, S. Ding, J. Schroers, J.J. Vlassak, Combining combinatorial nanocalorimetry and X-ray diffraction techniques to study the effects of composition and quench rate on Au–Cu–Si metallic glasses, *Scripta Materialia* **66**, 178–181 (2012)

## REFERENCES

[1]  W.L. Benard, H. Kahn, A.H. Heuer, M.A. Huff, Journal of Microelectromechanical Systems **7**, 245-251 (1998)

[2]  A.D. Johnson, Journal of Micromechanics and Microengineering **1**, 34-41 (1991)

[3]  M. Kohl, D. Dittmann, E. Quandt, B. Winzek, S. Miyazaki, D.M. Allen, Materials Science and Engineering A **273-275**, 784-788 (1999)

[4]  P. Krulevitch, A.P. Lee, P.B. Ramsey, J.C. Trevino, J. Hamilton, M.A. Northrup, Journal of Microelectromechanical Systems **5**, 270-282 (1996)

[5]  E. Makino, T. Mitsuya, T. Shibata, Sensors and Actuators A **88**, 256-262 (2001)

[6]  T. Mineta, N. Kida, S. Nomura, E. Makino, T. Sugawara, S. Toh, T. Shibata, Sensors and Actuators A **143**, 14-19 (2008)

[7]  Y. Fu, H. Du, W. Huang, S. Zhang, M. Hu, Sensors and Actuators A **112**, 395 (2004)

[8]  S. Sanjabi, Y.Z. Cao, S.K. Sadrnezhaad, Z.H. Barber, Journal of Vacuum Science and Technology A **23**, 1425-1429 (2005)

[9]  X.L. Meng, W. Cai, F. Chen, L.C. Zhao, Scripta Materialia **54**, 1599 (2006)

[10]  D.S. Grummon, JOM **55**, 24-32 (2003)

[11]  D.N. Abujudom, P.E. Thoma, M. Kao, D.R. Angst, High Transformation Shape Memory Alloy, in U. Patent, 5114504, United States, 1992

[12]  E.A. Olson, M. Yu, Y. Efremov, M. Zhang, Z.S. Zhang, L.H. Allen, Journal of Microelectromechanical Systems **12**, 355 (2003)

[13]  M. Hersscher: A micro differential scanning calorimetry system, Diploma Thesis, Albert-Ludwigs University, Freiburg, Germany (2003)

[13]  B. Revaz, B.L. Zink, F. Hellman, Thermochimica Acta **432**, 158 (2005)

[14]  A.A. Minakov, S.A. Adamovsky, C. Schick, Thermochimica Acta **432**, 177 (2005)

[15]  P.F. Sullivan, G. Seidel, Phys. Rev. **173**, 679 (1968)

[16]  S.F. Hsieh, S.K. Wu, Journal of Alloys and Compounds **266**, 276-282 (1998)

[17]  S.F. Hsieh, S.K. Wu, Materials Characterization **41**, 151-162 (1998)

[18]  W.J. Tang, Metallurgical and Materials Transactions A **28**, 537-544 (1997)

[19]  E. Cesari, P. Ochin, R. Portier, V. Kolomytsev, Y. Koval, A. Pasko, V. Soolshenko, Materials Science and Engineering A **273**, 738-744 (1999)

[20]  X. Wang: Diploma Thesis, Crystallization and Martensitic Transformation Behavior of NiTi Shape Memory Alloy Thin Films. Harvard University, Cambridge, Massachusetts, USA (2007)

[21]  T. Waitz, T. Antretter, F.D. Fischer, N.K. Simha, H.P. Karnthaler, Journal of the Mechanics and Physics of Solids **55**, 419-444 (2007)

[22] V.P. Sivokha, L.L. Meisner, Phys. B **296**, 329 (2001)

[23] H.Y. Kim, M. Mizutani, S Miyazaki, Acta Mater. **57**, 1920 (2009)

[24] K. Gall, H. Maier, Acta Mater. **50**, 4643 (2002)

[25] S. Miyazaki, A. Ishida, Mater. Sci. Eng. A **273**, 106 (1999)

[26] A. Ishida, V. Martynov, MRS Bull. **27**, 111 (2002)

[27] K. Otsuka, X. Ren, Prog. Mater. Sci. **50**, 511 (2005)

[28] S. Miyazaki, Y. Igo, K. Otsuka, Acta Metall. **34**, 2045 (1986)

[29] T. Simon, A. Kroger, C. Somsen, A. Dlouhy, G. Eggeler, Acta Mater. **58**, 1850 (2010)

[30] T. Waitz, V. Kazykhanov, H.P. Karnthaler, Acta Mater. **52**, 137 (2004)

[31] R. Zarnetta, R. Takahashi, M.L. Young, A. Savan, Y. Furuya, S. Thienhaus, B. Maass, M. Rahim, J. Frenzel, H. Brunke, Y.S. Chu, V. Srivastava, R.D. James, I. Takeuchi, G. Eggeler, A. Ludwig, Adv. Funct. Mater.20, 1917 (2010)

[32] S. Sanjabi, Y.Z. Cao, Z.H. Barber, Sens Actuators A **121**, 543 (2005)

[33] Y. Tong, Y. Liu, J. Miao, Thin Solid Films **516**, 5393 (2008)

[34] C.A. Schuh, T.C. Hufnagel, and U. Ramamurty, Acta Mater. **55**, 4067 (2007)

[35] W.H. Wang, C. Dong, C.H. Shek, Mater. Sci. Eng. R **44**, 45 (2004)

[36] M.F. Ashby, A.L. Greer, Scr. Mater. **54**, 321 (2006)

[37] J. Schroers, Adv. Mater. **22**, 1566 (2010)

[38] J.M. Gregoire, D. Dale, A. Kazimirov, F.J. DiSalvo, R.B. van Dover, Rev. Sci. Instrum. **80**, 123905 (2009)

[39] J.M. Gregoire, D. Dale, R.B. van Dover, Rev. Sci. Instrum. **82**, 015105 (2011)

[40] J. Schroers, B. Lohwongwatana, W.L. Johnson, A. Peker, Appl. Phys. Lett. **87**, 061912 (2005)

[41] P.J. McCluskey, J.J. Vlassak, Scr. Mater. **64**, 264 (2011)

[42] Y. Li, Q. Guo, J.A. Kalb, C.V. Thompson, Science **322**, 1816 (2008)

[43] Q. Hu, X.R. Zeng, M.W. Fu, J. Appl. Phys. **109**, 053520 (2011)

[44] T.D. Shen, U. Harms, and R.B. Schwarz, Appl. Phys. Lett. **83**, 4512 (2003)

[45] R. Busch, J. Schroers, and W.H. Wang, Mater. Res. Bull. **32**, 620 (2007)

[46] E.S. Park, D.H. Kim, Apply. Phys. Lett. **92**, 091915 (2008)

[47] A. Slipenyuk, J. Eckert, Scr. Mater. **50**, 39 (2004)

[48] A.L. Chamberlain, W.G. Fahrenholtz, G.E. Hilmas, J. Euro. Ceram. Soc. **29**, 3401 (2009)